MATERIALS SCIENCE

A biological nanofoam: The wall of coniferous bisaccate pollen

Ruxandra Cojocaru[1]†, Oonagh Mannix[1,2]†, Marie Capron[1,3]†, C. Giles Miller[4]†, Pierre-Henri Jouneau[5], Benoit Gallet[6], Denis Falconet[7], Alexandra Pacureanu[1]*, Stephen Stukins[4]*‡

The outer layer of the pollen grain, the exine, plays a key role in the survival of terrestrial plant life. However, the exine structure in different groups of plants remains enigmatic. Here, modern and fossil coniferous bisaccate pollen were examined to investigate the detailed three-dimensional structure and properties of the pollen wall. X-ray nanotomography and volume electron microscopy are used to provide high-resolution imagery, revealing a solid nanofoam structure. Atomic force microscopy measurements were used to compare the pollen wall with other natural and synthetic foams and to demonstrate that the mechanical properties of the wall in this type of pollen are retained for millions of years in fossil specimens. The microscopic structure of this robust biological material has potential applications in materials sciences and also contributes to our understanding of the evolutionary success of conifers and other plants over geological time.

INTRODUCTION

Pollen is the male gametophyte within the life cycle of typical gymnosperm and angiosperm plants, which evolved from spore-producing vascular land plant groups (Tracheophytes). Pollen grains, on the order of tens of micrometers in size, are the vessels for the transfer of generative cells between one parent plant and another; the protection they provide from external sources is vital to the survival of plants. For this purpose, the earliest land plants evolved a tough outer wall, produced from a highly resistant organic polymer, known as sporopollenin (*1*, *2*). The relatively inert nature of sporopollenin and its purported resistant structure allow it to protect the generative cell material from ultraviolet radiation, harsh temperature fluctuations, and other chemical and physical degradation. These properties are possibly the reason why the walls of spores and pollen are preserved in many sediments for millions of years, permitting paleontologists to study ancient floral histories in addition to the fossilized remains of plants. However, the exact chemical structure of sporopollenin is still debated (*3*–*7*).

This long-term preservation of pollen in sedimentary deposits permits comparison between modern and fossilized specimens to examine whether the properties of the pollen wall are retained over millions of years. Coniferous bisaccate pollen were chosen for this study as they are generally numerous, are cosmopolitan in distribution, range from several hundred millions of years ago to the present, and have interesting morphological features. The morphology of a common bisaccate coniferous pollen consists of a central body area (corpus), which contains the generative material, and two air bladders (sacci) at each end of the corpus (see Fig. 1A) (*8*).

This study focuses on the properties of the sporopollenin pollen wall. Other recent studies have tackled understanding of the inner structure of bisaccate pollen using modern imaging techniques (*9*–*11*). A previous x-ray diffraction experiment on the local structure of sporopollenin indicated that it is amorphous rather than crystalline (*12*). Using pine pollen, Li *et al.* (*5*) examined the molecular structure of sporopollenin, revealing a complex arrangement of components making up this biopolymer. While the chemistry of sporopollenin goes some way to explaining the preservation potential of the pollen wall, it is vital to look at the physical structure created to explain the properties that allow pollen to be preserved intact, in ancient sedimentary rocks for up to ≈425 million years (*13*) despite the high temperatures and pressures associated with burial and tectonic processes. The strength of the pollen wall has been confirmed in recent studies using supercritical carbon dioxide at 45 MPa for 10 min to break open the pollen grain (*14*).

Experiments on the scale of the pollen wall are challenging as the target of study is only ~1 μm thick. Hence, accessing the interior of the pollen wall would typically involve embedding the structure in resin and either using a focused ion beam or microtoming to isolate the material. Such destructive sample preparation is not appropriate for rare fossil samples, and even for modern samples has the disadvantage of potentially altering the material. Our study uses advanced imaging techniques to examine the unadulterated wall structure on the nanoscale.

X-ray holographic nanotomography (XNH) is used to produce high-resolution, three-dimensional (3D) reconstructions of modern bisaccate pollen. We report the inner structure of the pollen wall in the cappa region (the thickened upper surface between the two air sacs) as a solid nanofoam. The foam structure continues throughout the entire pollen wall, with average cavity sizes on the micrometer order around the two sacci.

Cellular foams known from nature include cork, bone, and sponge (*15*–*17*). The properties of foams, such as superior insulation, strength, and elasticity, are what make them common adaptations in the natural world (*16*, *18*). Until now, however, no biological material has been classified as a solid nanofoam, where the individual foam cells are on the nanometer (<1 μm) scale in size.

Atomic force microscopy (AFM) performed on the specimens provides data on the local mechanical properties of the pollen wall.

[1]ESRF—The European Synchrotron, 71 Avenue des Martyrs, Grenoble, France. [2]Helmholtz-Zentrum Berlin für Materialien und Energie GmbH, Hahn-Meitner-Platz 1, 14109 Berlin, Germany. [3]Partnership for Soft Condensed Matter, ESRF–The European Synchrotron, 71 Avenue des Martyrs, Grenoble, France. [4]Department of Earth Sciences, Natural History Museum, Cromwell Road, London SW7 5BD, UK. [5]Univ. Grenoble Alpes, CEA, IRIG-MEM, Grenoble, France. [6]Univ. Grenoble Alpes, CNRS, CEA, IRIG-IBS, Grenoble, France. [7]Univ. Grenoble Alpes, CNRS, CEA, INRAE, IRIG-LPCV, Grenoble, France.
*Corresponding author. Email: s.stukins@nhm.ac.uk (S.S.); joitapac@esrf.eu (A.P.)
†These authors contributed equally to this work.
‡Lead contact.

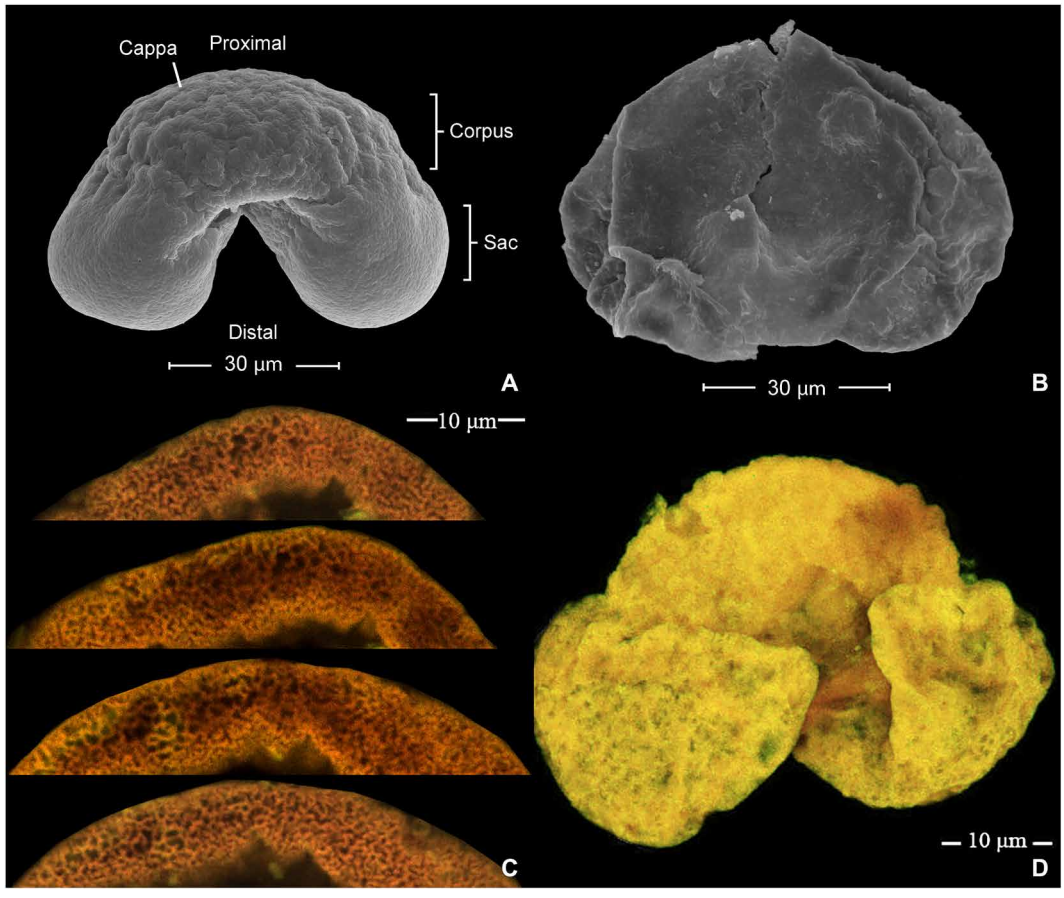

Fig. 1. SEM and confocal microscopy images of modern and fossil pollen grains. SEM images of (**A**) modern pine pollen in the lateral view and (**B**) fossil bisaccate pollen in the proximal view. Confocal microscopy measurements (**C**) of a modern pine pollen grain and (**D**) of a fossil bisaccate specimen. Eurugulate structures visible on modern pine are shown in (C) in different areas of the cappa at different focusing depths.

These are shown to be in the range of known values for other biological and synthetic foams. By comparing AFM results between both modern and fossil bisaccate pollen specimens, we show that the mechanical properties of the pollen wall are retained in fossils.

This novel quantitative characterization of the bisaccate pollen wall could further encourage its use as an applied biological material (*19*, *20*) and also as inspiration and as a biotemplate in the design of new materials (*21*–*24*).

RESULTS

Modern pine and fossil bisaccate pollen grains were investigated with multimodal and multiscale nanotechnologies: cryogenic XNH, AFM, cryogenic x-ray fluorescence (XRF) nanoimaging, focused ion beam scanning electron microscopy (FIB-SEM), and high-resolution transmission electron microscopy (HRTEM). An initial characterization of these materials was performed using SEM and confocal laser scanning microscopy (CLSM) to evaluate the correct identification, overall preservation, and microscopic structure of the specimens (Fig. 1).

Atomic force microscopy

AFM measurements were performed on both modern and fossil bisaccate samples. From tapping mode images, 3D figures of the measured samples were plotted and the amplitude and phase signals of the oscillation of the tip during scanning were measured. The phase signal provided information about the interaction between the tip and the sample. In addition to tapping images, mechanical measurements were performed, which produced force curves and force maps.

Each measurement consisted of scanning different areas of each specimen, starting with a larger scan of 10 µm × 10 µm down to a smaller 1 µm × 1 µm area. For each measurement, height and phase trace data were recorded, which were translated into visual maps. For smaller scanned areas, several point-by-point force maps following a rectangular grid were measured.

The surface roughness in the cappa region was computed from the height trace data obtained from 10 µm × 10 µm scans over different samples and different areas. Modern pine pollen specimens appear to be smoother, with an average roughness of ≈110 nm, whereas fossil specimens have a higher average roughness of ≈200 nm, which potentially suggests some degree of surface damage. Surface roughness is not uniform across the specimen.

AFM phase images show better contrast when compared to height trace images, thus allowing for an easier identification of different domains within the image. Here, this property is used to identify and measure individual cavities (cells) in the underlying foam-like structure forming the pollen wall (see example in Fig. 2). An average

cavity size of 106 nm × 72 nm (semi-major and semi-minor axes) was obtained with an average circularity of 75%.

AFM force curve mapping was performed on 3 μm by 3 μm areas on samples of both modern and fossil pollen specimens (Fig. 3). The goal of these measurements was to determine the Young's modulus (*E*), which is a mechanical property indicating the stiffness of a solid material. The force map mode was used to perform a statistical analysis of the mechanical properties present on the surface of the pollen grain. We measured 6 × 6 force maps, with a step size of 0.5 μm, for a scan size of 3 μm.

On the basis of the shape of the force curves and on plasticity values between 0.66 and 1.01, the Oliver-Pharr method was chosen to calculate the Young's modulus *E* in this study. This method was initially developed for indentation tests on shape memory samples (*25*, *26*). The resulting values for *E* vary across the surface of both the fossil specimen and the modern pollen, ranging from a few hundred megapascals to approximately 3 GPa (see Fig. 3, B and D). Figure S2 shows the corresponding adhesion force maps extracted from these measurements. The adhesion force ranges from 40 to 160 nN for modern pine pollen and from 50 to 420 nN for the fossil bisaccate sample. The broader distribution of the adhesion force values for the fossil sample can be attributed to its surface roughness being 50% higher than for the modern pine pollen (*27*).

X-ray nanotomography

X-ray phase-contrast holographic nanotomography measurements were performed on the modern pine pollen samples. Details regarding the experiment and the data processing are given in Materials and Methods. The technique enables the reconstruction of the 3D electron density distribution inside the samples with high precision (Fig. 4, A and B). These data reveal a foam- or sponge-like structure present throughout the entire pollen wall, although it is more prominently visible toward the outer edge of the pollen sacci.

The pollen wall, seen from outside-in, typically has several layers—a callosic wall, an exine, and an intine. For pine pollen, this layer distribution is typically found in the cappa region of the corpus, on the proximal part. The two sacci located on the distal side only present an exine wall, and the region between the sacci, where the pollen tube will emerge, presents a thin exine and a thick intine (*28*). Our data confirm this distribution, although contrast is insufficient to fully follow the callosic wall. However, the exine and intine can generally be distinguished.

Figure 4 (C and D) presents consecutive 2D XNH slices in the radial and transverse directions through a section of the pollen wall in the cappa region. The slices in the radial direction, taken every 800 nm, show what appear to be radial rods, connecting the upper and lower layers of the exine, with the upper layer being completely tectate or tectate-imperforate (*29*). These rod-like structures that connect the outer and inner surfaces of pollen wall can be interpreted as columellae, confirming an anisotropic trend in the development of the foam. The slices in transverse direction, taken every 200 nm, reveal that these structures are not actually rods, but eurugulate sculpture of varying size and curvature, with no particular orientation in this plane. They form an interconnected network of cavities, with larger cavity sizes in the sacci region as compared to the rest of the pollen. The quality of the data allows for a deeper microstructural characterization of the foam structure in the wall of the pollen grain.

The average cavity size, calculated as a Feret diameter, in the cappa region is approximately 500 nm. Toward the outer surface of the wall, the cavity size in the transverse plane averages 410 ± 240 nm, and toward the inner surface, the average increases to 510 ± 310 nm. In the sacci, the cavity size is on average 1.70 ± 1.39 μm.

FIB-SEM, TEM, and HRTEM

To further examine the structure of the pollen wall at finer levels, modern pine grains were prepared with high-pressure freezing followed by freeze substitution and staining, and imaged in 3D with FIB-SEM followed by targeted HRTEM. In parallel, samples from the same batch were prepared with standard chemical fixation and imaged with classical 2D TEM to generate a reference data type, which is already present in the literature (fig. S4).

The 3D FIB-SEM images, acquired at isotropic voxel sizes of 6 and 18 nm, show in fine detail the exine wall around the pollen grain, with a 3D structure similar to that seen in x-ray nanotomography (see extracted virtual slices in fig. S3). The intine, the lowermost layer of the pollen wall composed predominantly of cellulose and pectins, can be distinguished with a thickness of 191± 41 nm. The full dataset is made publicly available online to serve as resource for further investigations by the scientific community. HRTEM imaging of 70-nm-thick sections extracted from the exine confirms the amorphous atomic structure of the material (fig. S5).

DISCUSSION

This study has explored the structural and mechanical properties of the coniferous bisaccate pollen wall to prove that it represents a biologically occurring solid nanofoam. Here, we compare the mechanical

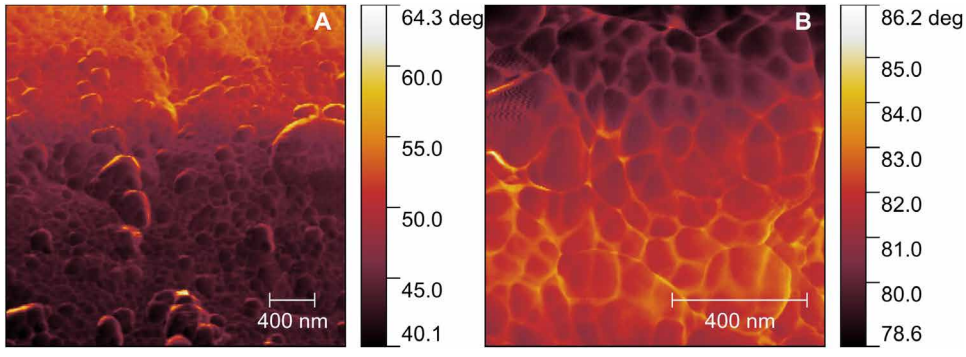

Fig. 2. AFM phase trace measurements on modern pine pollen grains. Phase trace data (**A**) over a 3 μm × 3 μm surface and (**B**) over a 1 μm × 1 μm surface.

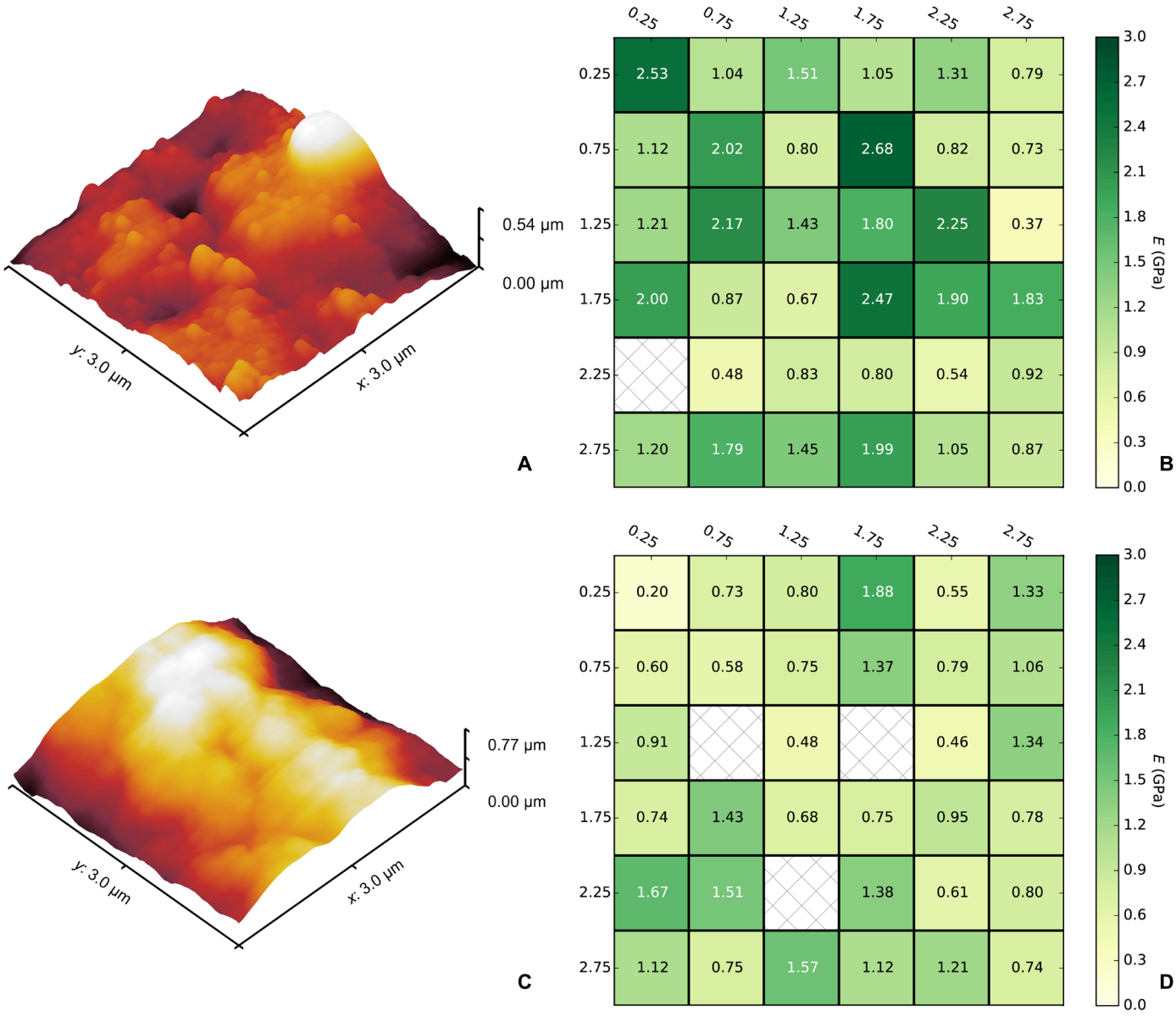

Fig. 3. AFM surface reconstructions and Young's modulus measurements obtained over 3 µm × 3 µm areas. (**A**) 3D surface reconstruction from height trace data from a modern pine pollen specimen. (**B**) Young's modulus values obtained using the Oliver-Pharr model on force map measurements from a 6 × 6 grid over the same area. The hatched boxes indicate grid points where the force curves were deemed unreliable due to a deficient contact between the tip and the surface. (**C** and **D**) Same type of data for a fossil bisaccate pollen specimen.

information obtained from AFM measurements with structural information obtained by nanoimaging techniques.

The AFM phase images (Fig. 2) from the surface of the cappa region of the specimens reveal an underlying cell-like structure, with individual cells of the size 106 nm × 72 nm on average. X-ray nanotomography measurements were used to further investigate this cell structure, thereby providing novel quantitative information and a detailed 3D understanding of the pollen wall structure on the nanoscale. The radial slices presented in Fig. 4C show rod-like structures connecting the outer and inner surfaces of the pollen wall, which could be interpreted as columellae. Transverse slices in Fig. 4D show no particular order in this plane and confirm an open eurugulate arrangement of variable size, curvature, and orientation. The eurugulate structures are also visible in the CLSM measurements (Fig. 1C). Such structures visible in 2D slices of the pollen wall have been well documented (*30*); however, the 3D data offer a better understanding of the true morphology within the exine.

The reconstruction obtained from x-ray nanotomography measurements indicates a larger 3D foam structure in the same region of the modern pine pollen specimen, ranging from an average cavity size of 410 nm toward the outer surface of the exine wall to 510 nm toward the proximal inner surface. Hints of foam-like cavities have previously been observed in high-resolution SEM micrographs (*20*) and x-ray tomography (*10*)—particularly in the sacci—and were

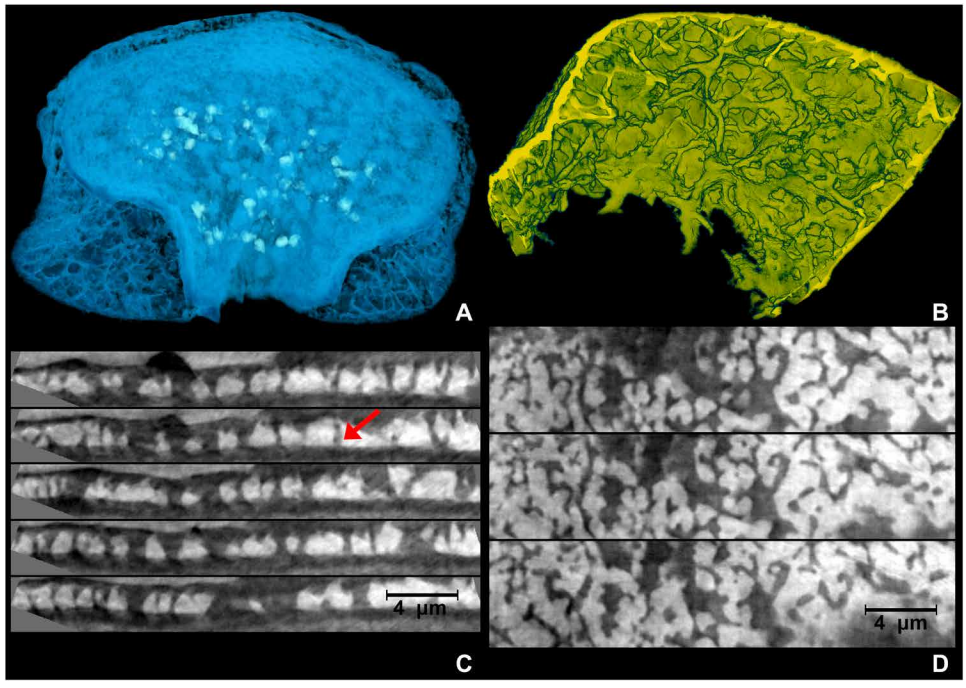

Fig. 4. 3D reconstruction of a modern pine pollen specimen from x-ray nanotomography data. (**A**) Lateral view of the full grain (see Fig. 1 for scale). (**B**) Zoom of the foam structure forming the wall of the pollen sac. (**C** and **D**) Slices from the tomographic reconstruction in the cappa region. In (C), five radial slices taken every 20 pixels (800 nm) through the structure of the exine wall illustrate vertical rod-like columella (example indicated by a red arrow), connecting the outer tectum and the inner foot layer (*30*). In (D), transverse slices taken every 5 pixels (200 nm) reveal detailed eurugulate structures.

described as "spongey" structures (*31*). To the authors' knowledge, this is the first time such cavities have been examined quantitatively and demonstrated to be present throughout the entire exine. It is this quantitative examination, made possible by the high resolution of the tomography data, that demonstrates definitively that the sporopollenin wall is organized as a solid nanofoam with increasing cavity size from the outer to the inner surface of the wall.

This is consistent with studies of naturally occurring solid microfoams such as cork and wood, which also show different properties in the radial and transverse directions (*17*). It is also consistent with studies of liquid foams, which present gravitational-induced anisotropy throughout their column (*32*). Solid nanofoams are typically synthetically produced and, depending on their fabrication technique, can show higher homogeneity and isotropy. However, the combination of low density, high strength, and high thermal insulation of foams (*16*, *18*) makes them the ideal natural adaptation for protecting the generative material within the pollen grain while keeping the pollen light enough for dispersal.

The nanotomography data were also used to determine the mass density of the sporopollenin exine. Density values ranged from 1.65 to 1.96 g cm^{-3}, with a mean of 1.76(10) g cm^{-3} and a porosity of about 70% (see also Fig. 5A). The density values are approaching those found in mineralized tissues such as human trabecular bone, a highly porous biological solid microfoam, with a tissue density of 1.87 g cm^{-3} (*33*) and an average porosity of 79.3% (*34*).

XRF measurements performed on modern pine pollen samples revealed that many trace elements are present within the cytoplasm and cell content encased within the pollen grain (see K distribution in Fig. 5C). However, Ca is present within the pollen wall itself (Fig. 5B). Ca could be a potential strengthening component much as it is in the construction of bones and industrial foam polymers and acts to reduce cell size and increase foam density (*35*).

X-ray nanotomography measurements were attempted on fossil bisaccate specimens, but the resulting contrast was insufficient to elucidate whether the pollen wall retained a nanofoam structure. This could be resolved in future experiments by embedding the specimens in a different resin to improve contrast.

The AFM data also provide information on the mechanical response of the pollen wall. The mechanical response of foams is usually dependent on the shape of the cavities and the density and nature of the solid (bulk) material of which the foam is made (*16*). For reference, a summary of the typical properties of both synthetic and natural foams is given in Table 1. For many such foams, the Young's modulus values are in the gigapascal range, indicating stiff materials; however, more flexible foams such as cork and PGMA have *E* values in the megapascal range. Biologically occurring solid foams typically have cavity sizes of tens or hundreds of micrometers, whereas synthetic foams can access the nanoscale range, as seen in Table 1.

The local values obtained for the Young's modulus *E* from AFM force curve measurements vary across the surface of both fossil and modern pollen, typically ranging from a few hundred megapascals to approximately 3 GPa (see examples in Fig. 3, B and D), suggesting an overall stiff and tough material. These values are consistent with those observed in other synthetic and natural materials as shown in Table 1. On average, the *E* values of the fossil specimens are somewhat lower and more variable from one specimen to another, which can be attributed to specimen preservation. However, the overall range of *E* values is similar for both the modern and fossil

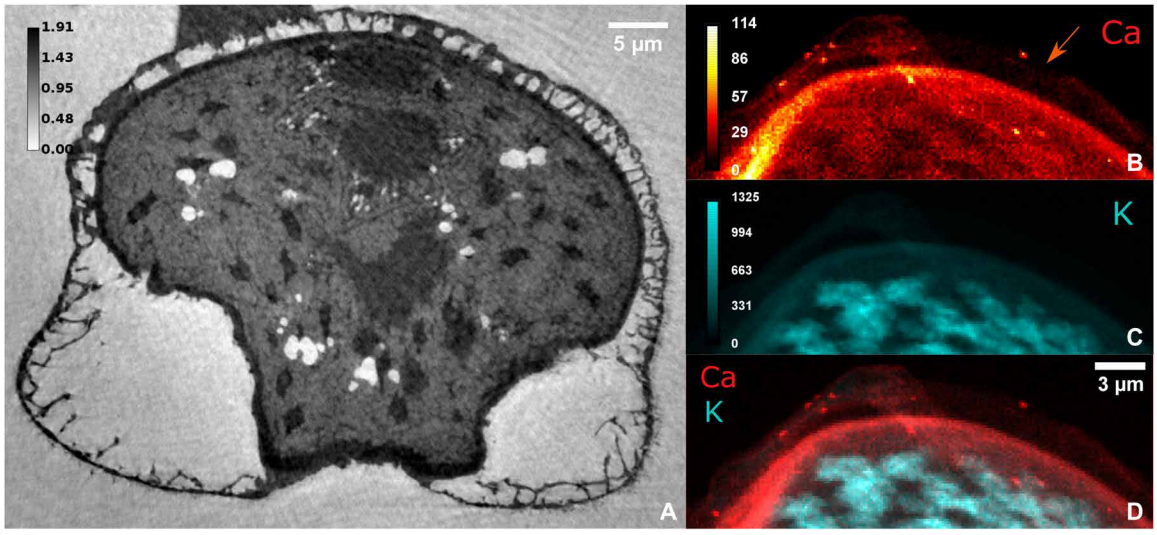

Fig. 5. Density distribution from x-ray nanotomography and XRF data showing Ca and K trace element distributions. (**A**) Slice from the reconstruction of a modern pine pollen specimen from nanotomography measurements. The gray map corresponds to mass density in [g cm^{-3}]. Following XRF measurements on the same specimen, on the upper right side of the grain oriented as shown in the previous panel, (**B**) and (**C**) present the distribution of Ca and K concentrations [ng mm^{-2}], respectively, within the pollen grain. There is a notable concentration of Ca contained in the foam structure of the pollen wall (indicated by an orange arrow), whereas elements such as K can be found in much higher quantities in the cytoplasm and cell contents present inside the grain. (**D**) Composite image showing both Ca (red) and K (blue) trace element distributions.

Table 1. Comparison of solid micro- and nanofoams of natural and synthetic origin. *E* is the Young's modulus of the material, and D_{cavity} is the average cell diameter. PC, polycarbonate; PMMA, polymethylmethacrylate; PGMA, polyglycidylmethacrylate.

Foam type	*E* (GPa)	D_{cavity} (µm)
Hardwood (*53*–*56*)	14.4	20–225
Trabecular bone (*57*, *58*)	10.4–14.8	13–40
Softwood (*53*, *54*, *59*)	13.1	10–50
Cork (*15*)	$7.9–13.2 \times 10^{-3}$	13–40
Microcellular PC (*60*)	0.75–2.65	8–5
PMMA (*61*)	1.1–1.9	0.3347–1.5
PGMA (*62*)	1.3×10^{-3}	≈0.1
Nanocellular PC (*60*)	1–2.9	$17–25 \times 10^{-3}$
Graphene nanofoam (*63*, *64*)	<36.6	$1.5–210 \times 10^{-3}$
Pine pollen wall cappa*	0.4–2.7	≈0.5
Fossil pollen cappa*	0.2–1.9	–

*This study.

pollen, which is notable, suggesting that the fossil samples retained their mechanical properties over 165 million years.

The shape of the force curves (see fig. S1 for an example), obtained from AFM measurements, is typical of a bending-dominated structure, followed by the fracturing of the cavity edges causing permanent deformation of the surface (*36*). During indentation tests when the stress rises substantially, the opposite sides of the cavities are forced into contact and further bending or buckling is not possible. After a second scan, we were not able to see an indent on the surface. This is explained by the underlying structure absorbing energy until the cell breaks. From AFM experiments, it is impossible to determine if the structure of the pollen wall is a closed or open cell nanofoam. However, the x-ray nanotomography measurements confirm that the foam presents an open/interconnected cavity architecture.

This study brings physical quantitative evidence that corroborates the hypothesis that the wall structure of bisaccate gymnosperm pollen grains represents a solid nanofoam. To our knowledge, this is the first reported biologically occurring solid nanofoam. This claim is supported by structural and mechanical properties derived from x-ray nanotomography, AFM, FIB-SEM, TEM, and HRTEM experiments. The HRTEM measurements indicate that the sporopollenin in the exine presents an amorphous structure.

In terms of future research, stress-strain tests could help further constrain the nature of the foam, as they would provide information on its linear elasticity and at which point the cell edges yield plastically, buckle, or fracture (*16*). It would also be of interest to repeat the x-ray nanotomography experiments on both fossil bisaccate specimens and other types of pollen to investigate in a more systematic manner whether other types of pollen present nanofoam wall structures, or whether this peculiar organization of sporopollenin is specific only to the formation process of bisaccate gymnosperm pollen.

From an evolutionary context, the nanofoam arrangement in the sporopollenin wall of gymnosperm pollen could potentially explain its resilience as a compound both in the modern environment and in the fossil record.

This new quantitative characterization of the bissacate pollen wall is important for applications, for example, pollen has been considered a natural possibility for drug encapsulation for some time now and pine pollen has recently been used for testing of this

application (*37*). The nanofoam structure may also inform studies that consider pollen as a model material used to fabricate and inspire biomimetic materials (*21*, *38*, *39*).

MATERIALS AND METHODS

Modern pollen

Modern Pinaceae (pine) pollen was collected from the region of Grenoble (France) in late February 2018 (for SEM, AFM, and x-ray nanotomography experiments) and late May 2021 (for FIB-SEM, TEM, and HRTEM measurements). The remaining sample material is registered at the Natural History Museum, London (*40*). The pollen grains were not processed with any chemical products for confocal microscopy, x-ray nanotomography, and XRF experiments; for SEM imaging and AFM measurements, the pollen was immersed in ethanol overnight to facilitate the direct measurement of the exine surface. The sample preparation for FIB-SEM, TEM, and HRTEM measurements is described in detail in the corresponding method sections.

Fossil pollen

The fossilized bisaccate pollen (*Pityosporites* spp.) was extracted from an organic residue prepared using acid digestion (HCl and HF) of mudrock. The mudrock was taken from location 1, bed 1 of Wakefield (1994) (*41*), Kildonnan Member, Lealt Shale Formation, Middle Jurassic on the Isle of Eigg. The residue is registered at the Natural History Museum, London (NHMUK PM BM 3751) (*40*). The fossilized pollen is composed of only the preservable sporopollenin exine due to the degradation of all other biological components during taphonomic processes.

Scanning electron microscopy

The external surfaces and whole grain morphology of modern and fossil pollen were investigated by SEM. Specimens were mounted as a distilled water–based strew on a glass coverslip attached to the surface of a standard 1-cm-diameter aluminum stub. The surface of each stub was coated with a 20-nm layer of gold-palladium alloy using a Cressington 208HR sputter coater. Specimens were then photographed with a Quanta 650 FEG SEM using a beam of 10 kV at a working distance of 20 mm and a chamber pressure of 2.37×10^{-3} Pa. Images confirmed the fossil pollen as *Pityosporites* spp., which is from a gymnosperm relative of the modern pine from which we collected the modern pollen (Fig. 1B).

Confocal laser scanning microscopy

The autofluorescence properties of the sporopollenin pollen wall allow for untreated observation of the specimens using CLSM. The CLSM was performed on the modern and fossil specimens taken from residue, mounted on a glass slide with a 0.18-mm coverslip and Glue4Glass mounting medium. A Nikon Eclipse upright with an A1-Si confocal microscope was used for imaging. The images were taken in epifluorescent mode using a Plan Apo VC 60× Oil DIC N2 DIC N2 objective. The z-stack data were acquired and analyzed using NIS-Elements software to create images of surface and internal features of the pollen wall. These include the gross morphology, with wall structure of the fossil specimen showing how well the pollen has preserved (Fig. 1D) and the eurugulate structure that the sporopollenin wall creates within the cappa region of the modern pollen grain (Fig. 1C).

Atomic force microscopy

AFM imaging was performed on both modern pine pollen and fossil bisaccate pollen specimens. The specimens were adhered to a flat mica surface using a commercially available brand of nail polish based on nitrocellulose and polyvinyl butyral resin. In situ AFM imaging was performed at room temperature (22°C) in tapping mode using an Asylum Research MFP-3D AFM instrument, from the Partnership for Soft Condensed Matter (PSCM), equipped with Oxford Instruments AC160TS-R3 silicon probes, with a resonance frequency of 279.5 kHz measured using the thermal noise method and a measured spring constant of 27 N m^{-1}. For force curve measurements, the scan rate was equal to 0.25 Hz and the trigger point was around 1.5 μm, which corresponds to a trigger force of 1.4 μN.

AFM height and phase images were preprocessed in Gwyddion, where the mean plane was subtracted from each image to flatten the surfaces. For surface roughness computations, height trace data were leveled by subtracting the mean plane and the polynomial fourth-order background, and then R_a and R_q(RMS) were computed. The phase images were analyzed in FIJI/ImageJ, where edge-enhancing techniques were used to better isolate the individual domains before applying a threshold to obtain a binary image. Last, the "Analyze particles" algorithm was used to identify individual cavities outlined on the pollen surface, by fitting each detected cavity with an ellipse. Force curve data were analyzed using the Asylum Research software and Igor. The final plots were produced via Python scripts. A full protocol describing the measurement and analysis is published (*42*).

X-ray nanotomography

X-ray phase-contrast holographic nanotomography (*43*) was performed at the ESRF beamline ID16A. This beamline offers a nanofocused x-ray beam of ≈20 nm combined with a large photon flux of 1.4×10^{12} photons/s (*44*). Measurements were performed at 17 keV, with a monochromaticity of $\Delta E/E = 1\%$. To preserve the specimen from radiation damage, data collection was done under cryogenic conditions (−160°C). Individual specimens were glued to a metallic tungsten tip, cut from a 125-μm-diameter wire, to ensure sample stability. They were then placed in the cryoloading system before being imaged in a high-vacuum 10^{-7} mbar chamber. With a diameter up to approximately 70 μm, the pollen grains were sometimes slightly larger than the field of view, which varied between 40 and 80 μm for voxel sizes of 20 to 40 nm; in these cases, several scans of different regions of interest were performed to cover the entire specimen.

The data were reconstructed using Octave custom code to obtain phase maps, and the tomographic volumes were computed using PyHST. 3D renderings were obtained using the ParaView software. The foam cavity size was determined in 10 different regions of the pollen wall (about 650 voxels across per region in the cappa and 1200 voxels across in the sacci) by adapting a postprocessing algorithm (*45*), originally used for open aluminum foams, using FIJI/ImageJ. The steps of this algorithm are similar to those described for analyzing the AFM phase trace images, but adapted for 3D data.

The density of the foam wall was retrieved from the tomographic reconstruction, measuring it in 20 different regions of the pollen wall (about 1500 voxels in total). The reconstruction gives the value of the optical path $\omega = -\frac{2\pi}{\lambda}\delta$, where $\lambda = 0.72727$ Å is the photon wavelength for an energy of 17.05 keV and δ is the phase difference. Using the Guinier approximation, $\delta = 1.310^{-6}\rho\,[\mathrm{g/cm^3}]\lambda^2\,[\mathrm{Å}]$ (*46*), and the density can be computed as

$$\rho\,[\mathrm{g/cm^3}] = -\frac{10^{-2}\omega\,[\mathrm{cm^{-1}}]}{1.3\lambda\,[\mathrm{Å}]2\pi} \quad (1)$$

Last, this value must be corrected by an offset, usually obtained by considering a region of known density in the reconstruction, for example, air. In this specific case, the vacuoles inside the pollen grain were the region of lowest density, so we considered these to be filled with air. If one were to consider a higher-density content inside the vacuoles, the determined density for the sporopollenin exine would be larger. A full protocol describing the measurement and analysis is published (*47*), and the raw data are openly available (*48*).

XRF measurements

Synchrotron-based XRF measurements (*49*) were performed on the modern pine pollen samples to quantify trace element concentrations down to the sub-ppm (parts per million) level. The measurements have been carried out within the same instrument as for the phase-contrast nanotomography. The excitation energy was 17 keV, the pixel size was 150 nm^2, and the dwell time was 50 ms. The resulting spectra were recorded with a silicon drift energy-dispersive detector and analyzed using PyMCA.

Focused ion beam SEM

Modern pine pollen grains were cryofixed using high-pressure freezing (HPM100, Leica), followed by freeze substitution (EM ASF2, Leica) (*50*, *51*). For the freeze substitution, a mixture of 2% (w/v) osmium tetroxide and 0.5% (w/v) uranyl acetate in dried acetone was used following the protocol from Decelle *et al.* (*50*), which is suitable for FIB-SEM imaging.

FIB-SEM observations were performed with a Zeiss Crossbeam 550 microscope on the cryofixed sample, with a protocol fully described in previous publications (*51*). The resin block containing the pollen was attached to a stub with carbon paint, its surface was abraded with an ultramicrotome to make it flat and clean, and then a thin (~3 nm) layer of platinum was applied.

When cut by a diamond knife, the pollen grains leave a thin trace on the surface, allowing the selection of areas of interest for 3D observations. For 3D acquisition, the sample was abraded slice by slice in cross section with a Ga^+ ion beam, at a current of 1.5 nA at 30 kV, and each freshly exposed surface is simultaneously imaged by SEM using a current of 1 nA at 1.5 kV with the in-lens backscattered electron detector. The thickness of abraded slices in FIB was chosen equal to the size of pixel in SEM to acquire isotropic voxels. Three volumes were acquired, with a voxel size of 6 nm × 6 nm × 6 nm (small field of view at high resolution) or 18 nm × 18 nm × 18 nm (for a larger field of view at lower resolution).

Transmission electron microscopy

Modern pine pollen grains were processed according to Flori *et al.* (*52*). Briefly, samples were washed in 0.1 M phosphate buffer (PB) (pH 7.4), fixed in a PB containing 2.5% (v/v) glutaraldehyde for 2 hours at room temperature, and stored overnight at 4°C. Samples were washed five times in PB and fixed by incubation on ice for an hour in a PB containing 2% osmium and 1.5% (w/v) ferricyanide potassium, followed by five washes with PB. Samples were resuspended in PB containing 0.1% (w/v) tannic acid and incubated for 30 min in the dark at room temperature. Samples were washed in PB, followed by dehydration in ascending washes of ethanol. Samples were infiltrated with an ethanol/Epon resin mixture and embedded in Epon. Ultrathin sections (50 to 70 nm) were prepared with a diamond knife on a PowerTome ultramicrotome and collected on 200-µm nickel grids. Last, ultrathin sections were examined on a JEOL 1200EX TEM operating at 80 kV.

High-resolution TEM

For high-resolution TEM observations, thin sections (~70 nm) of the same cryofixed sample were cut by ultramicrotomy and placed on a thin film of carbon supported by a standard TEM grid (Agar S160-3). TEM observations were carried out at 200 kV on a Thermo Fisher Scientific Titan Themis microscope equipped with a Cs Double corrector DCOR (CEOS) probe corrector, either in conventional TEM or in scanning TEM mode.

Image adjustments

In Figs. 1 and 4A, a dark mask was applied to frame the specimen and remove small background biologic debris. Labels, scale bars, and arrows were added to all images where useful. To comply with journal requirements, some images were scaled without interpolation to fulfill the requested digital image resolution of 600 ppi. All raw images are available online.

SUPPLEMENTARY MATERIALS

Supplementary material for this article is available at https://science.org/doi/10.1126/sciadv.abd0892

REFERENCES AND NOTES

1. C. H. Wellman, *The Evolution of Plant Physiology* (Elsevier, 2004), pp. 43–63.
2. E. Pacini, M. Hesse, Uncommon pollen walls: Reasons and consequences. *Verh. Zool. Bot. Ges. Osterr.* **148-149**, 291–306 (2012).
3. J. S. Watson, M. A. Sephton, S. V. Sephton, S. Self, W. T. Fraser, B. H. Lomax, I. Gilmour, C. H. Wellman, D. J. Beerling, Rapid determination of spore chemistry using thermochemolysis gas chromatography-mass spectrometry and micro-Fourier transform infrared spectroscopy. *Photochem. Photobiol. Sci.* **6**, 689–694 (2007).
4. P. E. Jardine, F. A. J. Abernethy, B. H. Lomax, W. D. Gosling, W. T. Fraser, Shedding light on sporopollenin chemistry, with reference to UV reconstructions. *Rev. Palaeobot. Palynol.* **238**, 1–6 (2017).
5. F.-S. Li, P. Phyo, J. Jacobowitz, M. Hong, J.-K. Weng, The molecular structure of plant sporopollenin. *Nat. Plants* **5**, 41–46 (2019).
6. A. Mikhael, K. Jurcic, C. Schneider, D. Karr, G. L. Fisher, T. D. Fridgen, A. Diego-Taboada, P. E. Georghiou, G. Mackenzie, J. Banoub, Demystifying and unravelling the molecular structure of the biopolymer sporopollenin. *Rapid Commun. Mass Spectrom.* **34**, e8740 (2020).
7. J.-S. Xue, B. Zhang, H. Zhan, Y.-L. Lv, X.-L. Jia, T. Wang, N.-Y. Yang, Y.-X. Lou, Z.-B. Zhang, W.-J. Hu, J. Gui, J. Cao, P. Xu, Y. Zhou, J.-F. Hu, L. Li, Z.-N. Yang, Phenylpropanoid derivatives are essential components of sporopollenin in vascular plants. *Mol. Plant* **13**, 1644–1653 (2020).
8. M. H. Kurmann, Pollen wall formation in *Abies concolor* and a discussion on wall layer homologies. *Can. J. Bot.* **67**, 2489–2504 (1989).
9. G. Kim, S. Lee, S. Shin, Y. Park, Three-dimensional label-free imaging and analysis of Pinus pollen grains using optical diffraction tomography. *Sci. Rep.* **8**, 1782 (2018).
10. Q. Li, J. Gluch, P. Krüger, M. Gall, C. Neinhuis, E. Zschech, Pollen structure visualization using high-resolution laboratory-based hard X-ray tomography. *Biochem. Biophys. Res. Commun.* **479**, 272–276 (2016).
11. J. W. Schopf, C. P. Calça, A. K. Garcia, A. B. Kudryavtsev, P. A. Souza, C. M. Félix, T. R. Fairchild, In situ confocal laser scanning microscopy and Raman spectroscopy of bisaccate pollen from the Irati Subgroup (Permian, Paraná Basin, Brazil): Comparison with acid-macerated specimens. *Rev. Palaeobot. Palynol.* **233**, 169–175 (2016).
12. Y. Wang, T. Len, Y. Huang, A. Diego Taboada, A. N. Boa, C. Ceballos, F. Delbecq, G. Mackenzie, C. Len, Sulfonated sporopollenin as an efficient and recyclable heterogeneous catalyst for dehydration of D-xylose and xylan into furfural. *ACS Sustain. Chem. Eng.* **5**, 392–398 (2017).
13. C. H. Wellman, P. L. Osterloff, U. Mohiuddin, Fragments of the earliest land plants. *Nature* **425**, 282–285 (2003).
14. X. Xu, L. Sun, J. Dong, H. Zhang, Breaking the cells of rape bee pollen and consecutive extraction of functional oil with supercritical carbon dioxide. *Innov. Food Sci. Emerg. Technol.* **10**, 42–46 (2009).
15. S. P. Silva, M. A. Sabino, E. M. Fernandes, V. M. Correlo, L. F. Boesel, R. L. Reis, Cork: Properties, capabilities and applications. *Int. Mater. Rev.* **50**, 345–365 (2005).
16. M. Ashby, The properties of foams and lattices. *Philos. Trans. A Math. Phys. Eng. Sci.* **364**, 15–30 (2006).

17. H. Pereira, The rationale behind cork properties: A review of structure and chemistry. *Bioresources* **10**, 6207–6229 (2015).
18. Y. Chen, R. Das, M. Battley, Effects of cell size and cell wall thickness variations on the stiffness of closed-cell foams. *Int. J. Solids Struct.* **52**, 150–164 (2015).
19. A. Diego-Taboada, S. T. Beckett, S. L. Atkin, G. Mackenzie, Hollow pollen shells to enhance drug delivery. *Pharmaceutics* **6**, 80–96 (2014).
20. A. K. Prabhakar, H. Y. Lai, M. G. Potroz, M. K. Corliss, J. H. Park, R. C. Mundargi, D. Cho, S.-I. Bang, N.-J. Cho, Chemical processing strategies to obtain sporopollenin exine capsules from multi-compartmental pine pollen. *J. Ind. Eng. Chem.* **53**, 375–385 (2017).
21. Y. Zhang, X. Li, P. Dong, G. Wu, J. Xiao, X. Zeng, Y. Zhang, X. Sun, Honeycomb-like hard carbon derived from pine pollen as high-performance anode material for sodium-ion batteries. *ACS Appl. Mater. Interfaces* **10**, 42796–42803 (2018).
22. Y. Xia, W. Zhang, Z. Xiao, H. Huang, H. Zeng, X. Chen, F. Chen, Y. Gan, X. Tao, Biotemplated fabrication of hierarchically porous NiO/C composite from lotus pollen grains for lithium-ion batteries. *J. Mater. Chem.* **22**, 9209–9215 (2012).
23. K. Xiao, T. Wang, M. Sun, A. Hanif, Q. Gu, B. Tian, Z. Jiang, B. Wang, H. Sun, J. Shang, P. K. Wong, Photocatalytic bacterial inactivation by a rape pollen-MoS_2 biohybrid catalyst: Synergetic effects and inactivation mechanisms. *Environ. Sci. Technol.* **54**, 537–549 (2020).
24. R. D. Ávila-Avilés, N. Torres-Gómez, M. A. Camacho-López, A. R. Vilchis-Nestor, SERS activity of hybrid nano/microstructures Ag-Fe_3O_4 based on *Dimorphotheca ecklonis* pollen grains as bio-template. *Sci. Rep.* **10**, 16633 (2020).
25. W. C. Oliver, G. M. Pharr, An improved technique for determining hardness and elastic modulus using load and displacement sensing indentation experiments. *J. Mater. Res.* **7**, 1564–1583 (1992).
26. W. C. Oliver, G. M. Pharr, Measurement of hardness and elastic modulus by instrumented indentation: Advances in understanding and refinements to methodology. *J. Mater. Res.* **19**, 3–20 (2004).
27. X. Jin, B. Kasal, Adhesion force mapping on wood by atomic force microscopy: Influence of surface roughness and tip geometry. *R. Soc. Open Sci.* **3**, 160248 (2016).
28. E. Pacini, G. G. Franchi, M. Ripaccioli, Ripe pollen structure and histochemistry of some gymnosperms. *Plant Syst. Evol.* **217**, 81–99 (1999).
29. J. M. Osborn, T. N. Taylor, *Ultrastructure of Fossil Spores and Pollen*, M. H. Kurmann, J. Doyle, Eds. (Royal Botanic Gardens, Kew, 1994), chap. 7, pp. 99–121.
30. W. Punt, P. P. Hoen, S. Blackmore, S. Nilsson, A. Le Thomas, Glossary of pollen and spore terminology. *Rev. Palaeobot. Palynol.* **143**, 1–81 (2007).
31. T. N. Taylor, E. L. Taylor, The ultrastructure of fossil gymnosperm pollen. *Bull. Soc. Bot. Fr. Actual. Bot.* **134**, 121–140 (1987).
32. C. Hill, J. Eastoe, Foams: From nature to industry. *Adv. Colloid Interface Sci.* **247**, 496–513 (2017).
33. R. Oftadeh, M. Perez-Viloria, J. C. Villa-Camacho, A. Vaziri, A. Nazarian, Biomechanics and mechanobiology of trabecular bone: A review. *J. Biomech. Eng.* **137**, 010802 (2015).
34. G. A. P. Renders, L. Mulder, L. J. Van Ruijven, T. M. G. J. Van Eijden, Porosity of human mandibular condylar bone. *J. Anat.* **210**, 239–248 (2007).
35. F.-C. Chiu, S.-M. Lai, C.-M. Wong, C. Hui Chang, Properties of calcium carbonate filled and unfilled polystyrene foams prepared using supercritical carbon dioxide. *J. Appl. Polym. Sci.* **102**, 2276–2284 (2006).
36. H.-J. Butt, B. Cappella, M. Kappl, Force measurements with the atomic force microscope: Technique, interpretation and applications. *Surf. Sci. Rep.* **59**, 1–152 (2005).
37. A. K. Prabhakar, M. G. Potroz, E.-L. Tan, H. Jung, J. H. Park, N.-J. Cho, Macromolecular microencapsulation using pine pollen: Loading optimization and controlled release with natural materials. *ACS Appl. Mater. Interfaces* **10**, 28428–28439 (2018).
38. X. Zhang, M. Ping, Z. Wu, C. Y. Tang, Z. Wang, Microfiltration membranes modified by silver-decorated biomimetic silica nanopollens for mitigating biofouling: Synergetic effects of nanopollens and silver nanoparticles. *J. Membr. Sci.* **597**, 117773 (2020).
39. T.-F. Fan, S. Park, Q. Shi, X. Zhang, Q. Liu, Y. Song, H. Chin, M. Shahrudin Bin Ibrahim, N. Mokrzecka, Y. Yang, H. Li, J. Song, S. Suresh, N. Cho, Transformation of hard pollen into soft matter. *Nat. Commun.* **11**, 1449 (2020).
40. R. Cojocaru, O. Mannix, M. Capron, A. Pacureanu, C. G. Miller, S. Stukins, Dataset: A biological nano-foam: The wall of coniferous bisaccate pollen. Natural History Museum Data Portal (2021); https://doi.org/10.5519/nahesy6w.
41. M. Wakefield, *Middle Jurassic (Bathonian) Ostracoda from the Inner Hebrides, Scotland* (Monograph of the Palaeontographical Society, 1994).
42. M. Capron, R. Cojocaru, O. Mannix, S. Stukins, AFM measurements on pollen sample, Protocols.io, Workflow (2021); https://dx.doi.org/10.17504/protocols.io.bn37mgrn.
43. M. Hubert, A. Pacureanu, C. Guilloud, Y. Yang, J. C. da Silva, J. Laurencin, F. Lefebvre-Joud, P. Cloetens, Efficient correction of wavefront inhomogeneities in x-ray holographic nanotomography by random sample displacement. *Appl. Phys. Lett.* **112**, 203704 (2018).
44. J. Cesar da Silva, A. Pacureanu, Y. Yang, S. Bohic, C. Morawe, R. Barrett, P. Cloetens, Efficient concentration of high-energy X-rays for diffraction-limited imaging resolution. *Optica* **4**, 492 (2017).
45. K. Schladitz, C. Redenbach, T. Sych, M. Godehardt, Microstructural characterisation of open foams using 3D images. *Berichte des Fraunhofer ITWM* **148**, (2008).
46. A. Guinier, *X-ray Diffraction—In Crystals, Imperfect Crystals, and Amorphous Bodies*, P. Lorrain, D. Lorrain, Transl. (Freeman and Company, 1964).
47. A. Pacureanu, R. Cojocaru, O. Mannix, ID16A measurements on pollen samples, Protocols.io, Workflow (2021); https://dx.doi.org/10.17504/protocols.io.bpfwmjpe.
48. R. Cojocaru, O. Mannix, M. Capron, A. Pacureanu, C. G. Miller, S. Stukins, Dataset: A biological nano-foam: The wall of coniferous bisaccate pollen, European Synchrotron Radiation Facility (ESRF) (2021); https://doi.org/10.15151/esrf-dc-339743082.
49. C. Gramaccioni, Y. Yang, A. Pacureanu, N. Vigano, A. Procopio, P. Valenti, L. Rosa, F. Berlutti, S. Bohic, P. Cloetens, Cryo-nanoimaging of single human macrophage cells: 3D structural and chemical quantification. *Anal. Chem.* **92**, 4814–4819 (2020).
50. J. Decelle, H. Stryhanyuk, B. Gallet, G. Veronesi, M. Schmidt, S. Balzano, S. Marro, C. Uwizeye, P.-H. Jouneau, J. Lupette, J. Jouhet, E. Maréchal, V. Schwab, N. L. Schieber, R. Tucoulou, H. Richnow, G. Finazzi, N. Musat, Algal remodeling in a ubiquitous planktonic photosymbiosis. *Curr. Biol.* **29**, 968–978.e4 (2019).
51. C. Uwizeye, M. M. Brisbin, B. Gallet, F. Chevalier, C. LeKieffre, N. L. Schieber, D. Falconet, D. Wangpraseurt, L. Schertel, H. Stryhanyuk, N. Musat, S. Mitarai, Y. Schwab, G. Finazzi, J. Decelle, Cytoklepty in the plankton: A host strategy to optimize the bioenergetic machinery of endosymbiotic algae. *Proc. Natl. Acad. Sci. U.S.A.* **118**, e2025252118 (2021).
52. S. Flori, P.-H. Jouneau, B. Gallet, L. F. Estrozi, C. Moriscot, G. Schoehn, G. Finazzi, D. Falconet, Imaging plastids in 2D and 3D: Confocal and electron microscopy. *Methods Mol. Biol.* **1829**, 113–122 (2018).
53. D. Guitard, F. E. Amri, Modèles prévisionnels de comportement élastique tridimensionnel pour les bois feuillus et les bois résineux. *Ann. For. Sci.* **44**, 335–358 (1987).
54. B. Thibaut, J. Gril, M. Fournier, Mechanics of wood and trees: Some new highlights for an old story. *C. R. Acad. Sci. IIB Mec.* **329**, 701–716 (2001).
55. M. T. Tyree, M. H. Zimmermann, *Xylem Structure and the Ascent of Sap* (Springer, ed. 2, 2002).
56. M. Capron, P. Tordjeman, F. Charru, E. Badel, H. Cochard, Gas flow in plant microfluidic networks controlled by capillary valves. *Phys. Rev. E* **89**, 033019 (2014).
57. T. Doktor, J. Valach, D. Kytyr, O. Jiroušek, Pore size distribution of human trabecular bone—Comparison of intrusion measurements with image analysis, in *Proc. 17th International Conference Engineering Mechanics*, Svratka, Czech Republic, 9 to 12 May 2011.
58. J. Y. Rho, R. B. Ashman, C. H. Turner, Young's modulus of trabecular and cortical bone material: Ultrasonic and microtensile measurements. *J. Biomech.* **26**, 111–119 (1993).
59. M. Havimo, J. Rikala, J. Sirviö, M. Sipi, Tracheid cross-sectional dimensions in Scots pine (*Pinus sylvestris*)—Distributions and comparison with Norway spruce (*Picea abies*). *Silva Fenn. (Hels.)* **43**, 681–688 (2009).
60. H. Guo, "Solid-state polymer nanofoams," thesis, University of Washington (2015).
61. J. Syurik, R. Schwaiger, P. Sudera, S. Weyand, S. Johnsen, G. Wiegand, H. Hölscher, Bio-inspired micro-to-nanoporous polymers with tunable stiffness. *Beilstein J. Nanotechnol.* **8**, 906–914 (2017).
62. Y. Galabura, A. P. Soliani, J. Giammarco, B. Zdyrko, I. Luzinov, Temperature controlled shape change of grafted nanofoams. *Soft Matter* **10**, 2567–2573 (2014).
63. H.-C. Tao, S.-C. Zhu, X.-L. Yang, L.-L. Zhang, S.-B. Ni, Systematic investigation of reduced graphene oxide foams for high-performance supercapacitors. *Electrochim. Acta* **190**, 168–177 (2016).
64. A. Pedrielli, S. Taioli, G. Garberoglio, N. M. Pugno, Mechanical and thermal properties of graphene random nanofoams via molecular dynamics simulations. *Carbon* **132**, 766–775 (2018).

Acknowledgments: We are grateful to staff of beamline ID16A and the microimaging laboratory for support before and during the nanoimaging experiments. We would like to thank the PSCM for access to laboratories and P. Lloria, A. Panzarella, and D. Pontoni for technical support. We are grateful to T. Góral for offering training and help with the CLSM and SEM measurements at the NHM. We would like to thank M. Majkut, J.-P. Suuronen, and S. Berujon for useful discussions. M.C. thanks G. Oliver from RNSA for offering information about pollination periods. S.S. thanks H. Bonney for useful discussion about the properties of bone. The Helmholtz Metadata Collaboration Hub Matter is thanked for assistance with data curation. This work used the platforms of the Grenoble Instruct-ERIC centre (ISBG; UMS 3518; CNRS-CEA-UGA-European Molecular Biology Laboratory) within the Grenoble Partnership for Structural Biology. We thank Guy Schoehn, Christine Moriscot, and the electron microscopy facility, which is supported by the Auvergne-Rhône-Alpes Region, the Fondation Recherche Medicale, the FEDER (Fonds européen de développement régional) and the GIS-Infrastructures.
Funding: We acknowledge ESRF for granting beamtime for the X-ray nano-imaging experiments (proposal EV-314 at beamline ID16A). The FIB-SEM, TEM and HRTEM measurements were supported by the French Infrastructure for Integrated Structural Biology (FRISBI) (ANR-10-INBS-05-02) and GRAL, financed within CBH-EUR-GS (ANR-17-EURE-0003).
Author contributions: R.C., O.M., and S.S. conceptualized the study. All authors contributed

to sample collection and preparation. C.G.M. was responsible for SEM measurements, S.S. for CLSM, M.C. for AFM, and A.P. for X-ray nanoimaging and reconstructions. B.G. and D.F. prepared samples for the various electron microscopy measurements. D.F. performed TEM on the chemically fixed sample. P.-H.J. collected and reconstructed FIB-SEM and HRTEM data. R.C., O.M., M.C., and A.P. performed data analysis and visualization. All authors contributed to data interpretation, manuscripting writing and manuscript revision. **Competing interests:** The authors declare that they have no competing interests. **Data and materials availability:** All raw data pertaining to the ID16A experiments are publicly available from the ESRF ICAT, DOI: doi.org/10.15151/esrf-dc-339743082 (*48*). Users can access the raw data by signing in as an anonymous user. Analyzed and curated data are available from the EMPIAR repository with the public accession code EMPIAR-10903. The samples used in this study have been registered with permanent identifiers in the database of the Natural History Museum, London, DOI: doi.org/10.5519/nahesy6w (*40*).

Submitted 31 May 2020
Accepted 15 December 2021
Published 9 February 2022
10.1126/sciadv.abd0892

ScienceAdvances

A biological nanofoam: The wall of coniferous bisaccate pollen

Ruxandra Cojocaru, Oonagh Mannix, Marie Capron, C. Giles Miller, Pierre-Henri Jouneau, Benoit Gallet, Denis Falconet, Alexandra Pacureanu, and Stephen Stukins

Sci. Adv., **8** (6), eabd0892.
DOI: 10.1126/sciadv.abd0892

Science Advances (ISSN) is published by the American Association for the Advancement of Science. 1200 New York Avenue NW, Washington, DC 20005. The title *Science Advances* is a registered trademark of AAAS.